Micro-Scale Propulsion using Multiple Flexible Artificial Flagella

John Singleton, Eric Diller, Tim Andersen, Stéphane Regnier, and Metin Sitti

Abstract— We propose a method to increase propulsion of a micro-scale swimming robot powered by an artificial flagellum through the use of multiple helices while retaining the simple actuation method of a single rotation axis. Scaled up experiments with similar Reynolds number are carried out to compare the performance of five different propulsion designs with pairs of stiff or flexible flagella. The designs feature stiff helices, straight flexible rods, and flexible helices inspired by bacterial flagella. Results indicate that for a given rotation frequency, thrust is proportional to the number of helices, but that the torque required to drive a flagellum offset from the common rotation axis is increased. Furthermore, shape deformation of flexible helices due to bending forces can positively affect thrust under certain conditions. Therefore, given the ease of fabrication, the use of multiple offset flexible flagella is a potential method to achieve increased thrust force in artificial bacteria flagella.
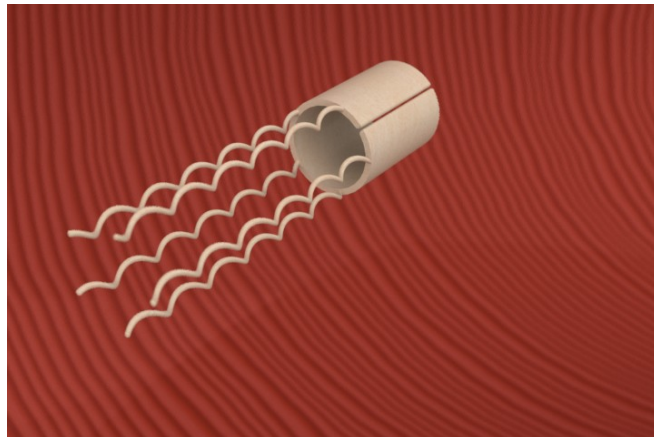
Fig. 1. Concept sketch of the proposed micro-scale propulsion system with multiple flexible flagella protruding downwards from the perimeter of the cylindrical body.

I. INTRODUCTION

Micro-scale swimming robots are attractive for biological and biomedical applications because much of the human body is filled with fluids. Some of the potential biomedical applications for swimming micro-robots are kidney stone removal, minimally invasive surgery, early stage disease screening, biopsy, and highly localized drug delivery [1]–[3].

Microorganisms swim with beating cilia or helical flagella, which are efficient due to the nature of fluid dynamics at the small scale. An example of helical flagella propulsion is found in prokaryotic *E. coli* and *S. marcescens*. The use of multiple flagella generates greater thrust force for these microorganisms. Many flagella are distributed randomly over the surfaces of these single cell organisms, with each flagellum rotated independently of the others by its own reversible biological motor. Due to hydrodynamic interactions, neighboring flagella that are turning counterclockwise bundle into a helical group behind the cell as it swims. The bacteria take advantage of this bundling effect to navigate using a series of "runs" and "tumbles". During a run, the flagella bundle and produce a coordinated thrust in one direction. When the motors of one or more flagella reverse, unbundling occurs and the cell tumbles, randomizing its direction. Varying the durations of the runs and tumbles allows the bacterium to effectively steer in three dimensions [4].

Untethered swimming micro-robot prototypes have been demonstrated and are actuated by rotating magnetic fields [5] or chemical reactions [6]. Abbott *et al.* [7] compare the

J. Singleton, E. Diller, T. Andersen and M. Sitti are with the Department of Mechanical Engineering, Carnegie Mellon University, Pittsburgh, PA 15213, USA [jsinglet, ediller, msitti]@andrew.cmu.edu

S. Regnier is with the Institute of Intelligent Systems and Robotics, Univ. Pierre et Marie Curie, Paris, France regnier@isir.upmc.fr

performance of several methods of propulsion at the micro-scale including a helical propeller rotated by a magnetic field, a flexible tail attached to a magnetic head, and a simple magnet pulled by a magnetic field gradient. They find that the helical propeller and elastic tail are both preferable to magnetic pulling when considering the limitations of magnetic field sources. Furthermore, this preference remains as micro-robot size decreases or as distance from the magnetic field source increases. Requiring only rotary motion for actuation, a flagellum serves as a relatively simple propulsion method, which is especially important for micro-robotics considering the difficulties associated with micro-scale fabrication.

Swimming using a single artificial flagellum has been explored by many research groups. Behkam *et al.* [1] compare the performance of various helical flagella, showing that force, torque, velocity, and efficiency of such swimmers are functions of geometry only. Micro/nanofabrication techniques have been developed to make helices attached to magnetic heads at a very small scale. For example, Zhang *et al.* [5] demonstrate a magnetic nanocoil 3 μm in diameter and 40 μm in length and Ghosh *et al.* [8] demonstrate nanoscale magnetic helices only 1 μm in length.

To increase the thrust of a micro-robot propelled by flagellar propulsion, we propose using multiple flagella in parallel [2] as shown conceptually in Fig. 1. Multiple micron scale flagella are proposed to be made parallel to each other on a hollow or solid cylinder. This is different from the biological analogue, which requires that each flagellum be rotated independently, because here the cylinder is rotated as a whole. The reasons for this are that rotating each flagellum independently is more difficult, and that multiple independently rotating flagella in close proximity have been

shown to negatively affect thrust [9]. The proposed cylinder would be rotated by magnetic actuation.

This paper gives analytical and experimental results for four different designs of the described multi-flagella system. The tested designs include stiff helices, flexible rods, and flexible helices. It is shown that flexible helices perform the best under certain conditions by combining the benefits of bending with those of helical geometry. It is also found that while the offset flagella require increased input torque for actuation, they represent a potential method for increasing thrust over the single-flagellum case.

II. Modeling

The model of thrust force of the offset flagella is adapted from a previously developed model for a single helix [1]. The propulsive force in the z direction, in terms of its longitudinal and normal components, is

$$dF_z = dF_l \cos \beta - dF_n \sin \beta, \tag{1}$$

where β is the constant pitch angle of the flagellum, defined as

$$\tan \beta = \frac{2\pi}{\lambda} A. \tag{2}$$

Here, λ is the flagella helix wavelength and A is the individual flagella amplitude as shown in Fig. 2(a).

Resistive force theory states that the normal and longitudinal forces acting on a cylindrical element of length ds are

$$dF_n = C_n V_n ds \quad \text{and} \tag{3}$$
$$dF_l = C_l V_l ds, \tag{4}$$

where V_n and V_l are respectively the normal and tangential velocities of the element and C_n and C_l are coefficients of resistance for a flagellum defined as [4]

$$C_n = \frac{4\pi\mu}{\ln\left(\frac{0.18\lambda}{d}\right) + \frac{1}{2}} \quad \text{and} \tag{5}$$
$$C_l = \frac{2\pi\mu}{\ln\left(\frac{0.18\lambda}{d}\right)}. \tag{6}$$

Here, μ is the fluid's dynamic viscosity and d is the flagellum wire diameter.

Because the flagella in our system are offset from the axis of rotation, V_n and V_l are not constant along the helix as in the single-helix case. Fig. 2(b) depicts the relative velocity vectors $\vec{u}$ of the fluid contacting a single offset flagellum. Relevant dimensions include R, the flagella offset distance, ω, the rotation frequency, and θ, the angle between $\vec{u}$ and $\vec{ds}$.

Since we are trying to find the forces on a single helix, we may orient it for our convenience. Choosing the rotation axis to be at (x, y) position $(0, 0)$ and the flagellum's center to be at $(R, 0)$, θ is then found by taking the difference between the tangent of the circle of radius R centered at the origin and the circle of radius A centered at $(R, 0)$. This gives

$$\theta = \tan^{-1}\left(-\frac{r_x}{r_y}\right) - \tan^{-1}\left(-\frac{r_x - R}{r_y}\right), \tag{7}$$
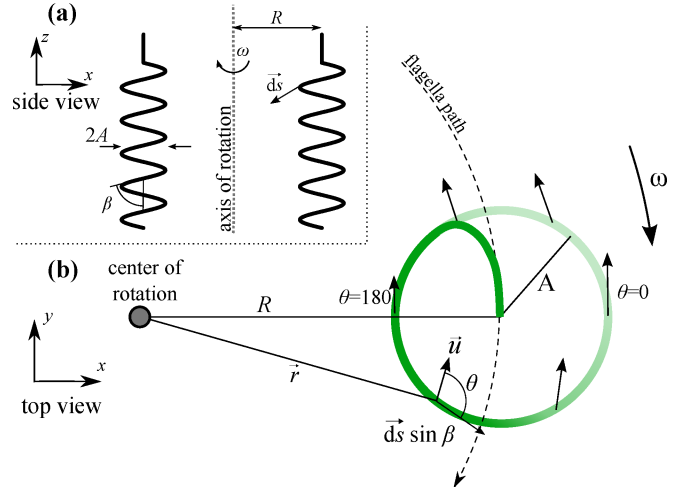

Fig. 2. Schematic of the offset flagella. (a) Side view of two offset artificial flagella with dimensions labelled. (b) A top down view of a single flagellum with a counter-clockwise helix rotating around an axis that is distance R away from its center of rotation. The vectors $\vec{u}$ are the relative fluid velocity vectors incident on the helix.

where $\vec{r} = (r_x, r_y)$ is a point on the flagellum. The fluid hits this point with velocity

$$\vec{u} = \vec{\omega} \times \vec{r}. \tag{8}$$

The component of this velocity tangent to the filament in the x-y plane is

$$\vec{u}_\theta = \vec{u} \cdot \vec{ds}. \tag{9}$$

This definition for $\vec{u}_\theta$ is now substituted into the model found in [1] with the forward velocity removed because the experiments performed measure the thrust of an artificial flagella held stationary. With $V_n = |\vec{u}_\theta| \cos \beta$, $V_l = |\vec{u}_\theta| \sin \beta$, and $ds = -\sec \beta\, dz$ the total propulsive force after manipulation is

$$\vec{F}_z = \int_0^{n\lambda} \vec{u}_\theta \sin \beta (C_n - C_l) dz. \tag{10}$$

When the flagella offset radius $R = 0$ the model correctly reduces to the case of one helix centered on the axis of rotation. This model does not include wall or fluidic coupling effects from neighbouring flagella. While it is not immediately apparent in (10), F_z does not vary with R due to cancellation of positive and negative forces. This result leads us to the conclusion that the thrust force for an offset rigid flagella should be the same as a flagella rotating about its center. This idea is illustrated in Fig. 3. The translation motion shown in the figure represents additional drag on the flagella which is not encountered with a single flagella rotating about its own axis.

It should be noted that because the experiments are performed in a highly viscous fluid, wall effects are significant despite the large size of the tank. It has been shown that wall effects are significant for $Re < 1$ when a body with characteristic length l is within $20l/Re$ distance of the wall, and that walls increase the observed propulsive force of the system [1]. This means that the experimental values will be
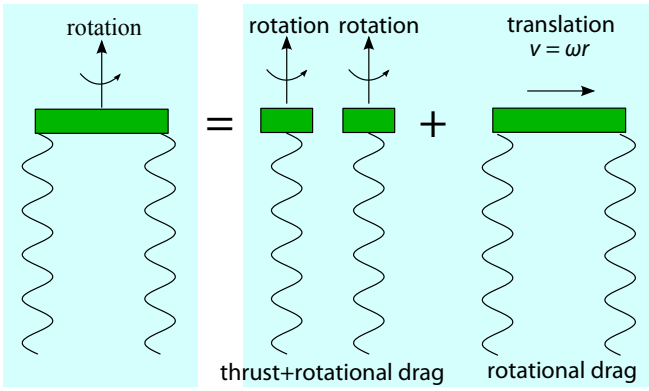
Fig. 3. Due to the linearity of flow at low Reynolds numbers, the thrust and drag produced by a pair of offset spinning flagella can be treated as a superposition of that produced by two single flagella rotating about their own axes and two flagella translating with velocity $V = \omega r$. This is only valid for rigid flagella; the case of flexible flagella introduces non-linear bending effects.
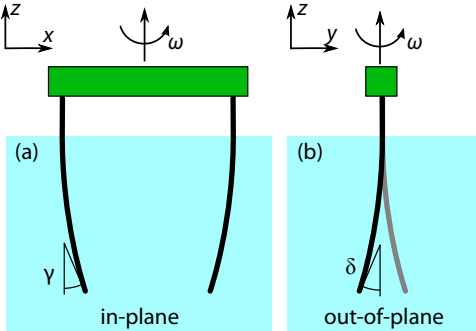

Fig. 4. Illustration of the bending angles experienced by the flexible rods, showing both in-plane bending (a) and out-of-plane bending (b).

higher than those from (10), which assumes an infinite fluid. To account for wall effects, (10) is multiplied by a correction term of [10]

$$\frac{C^*}{C_\infty} = \left(1 - \frac{2.1044 C_\infty l}{6\pi\mu h}\right)^{-1}, \qquad (11)$$

where C_∞ is the resistance coefficient without the presence of walls, C^* is the resistance coefficient adjusted for significant wall effects, and h is the distance to the wall.

It is clear that the unmodeled bending of the rods or helices due to the high viscous forces greatly affects thrust. Two modes of flexible rod and helix bending are visually observed on high speed camera: in plane, and out of plane, as shown in Fig. 4. In plane bending is when the filaments bend towards the axis of rotation. Out of plane bending is when the filaments bend backwards due to rotation. It is clear that these bending angles are related to rotation frequency, as well as the stiffness of the filaments.

Additionally, the equations presented in this section neglect fluidic coupling or interference effects between multiple flagella. We expect that the addition of more flagella in close proximity would negatively affect thrust, limiting the design to only a small number of parallel elements [9].
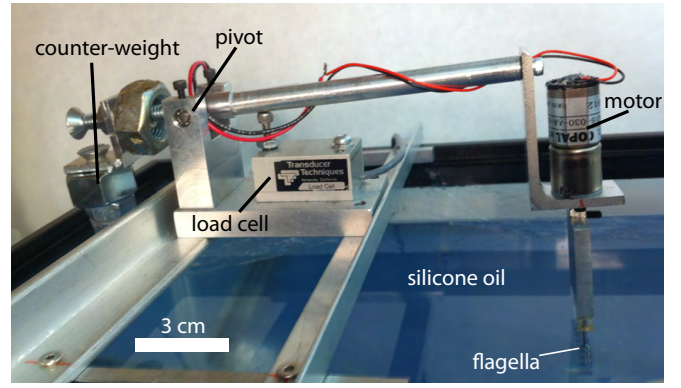

Fig. 5. Photo of the experimental setup.

III. EXPERIMENTS

Macro scale experiments are performed at similar Reynolds number as the planned micro-robot would experience so that results are scalable. Thrust data are collected using a cantilever and load cell system, shown in Fig. 5. The cantilever is balanced so that the load cell (Transducer Tech. model GSO-50) is lightly compressed when the helices are submerged into the 30,000 cSt silicone fluid (Clearco). The tank holding the oil is 215 mm wide by 400 mm long by 300 mm deep. The helices tested are driven through direct connection to a 30:1 geared DC motor (Copal model HG16-030-AA). With the motor running, the helices produce thrust to lift the cantilever, thus decompressing the load cell. The difference in the load cell signal when compressed and decompressed is multiplied by a calibrated term to convert to force at the flagella mounting point. The result is taken as the propulsive force of the system being tested. Data from the load cell is recorded through a data acquisition board (National Instruments PCI6024E) attached to a PC. Each experiment consists of recording the following cycle: motor off for 15 s, motor on for 40 s, motor off for 15 s. The 'motor off' portions are taken as baseline readings. Only the last 30 s of the 'motor on' portion is taken as the propulsive force data so that the system has ample time to reach equilibrium. The actual rotation frequency is extracted from characteristic artefacts in the load cell data from unbalance in the mounting. Experimental video is available in supplementary materials.

A. Fabrication

Five propulsion system designs are tested, with properties listed in Table I. The sixth design is a control design, with the expectation being that it produces no thrust because the rod is stiff enough to resist bending. The helices, shown in Fig. 6, are made by stretching and deforming steel springs to the desired dimensions. All of the helices are made with amplitude $A = 1.88$ mm, wavelength $\lambda = 5.10$ mm, and total length 15.40 mm.

The drive motor is rigidly attached to the cantilever system to allow only vertical motion. At steady state, the combination of the thrust of the helices, the opposing force from the load cell, and the counter weight are balanced with

TABLE I

DESIGNS USED IN THE EXPERIMENTS AND THEIR PROPERTIES.

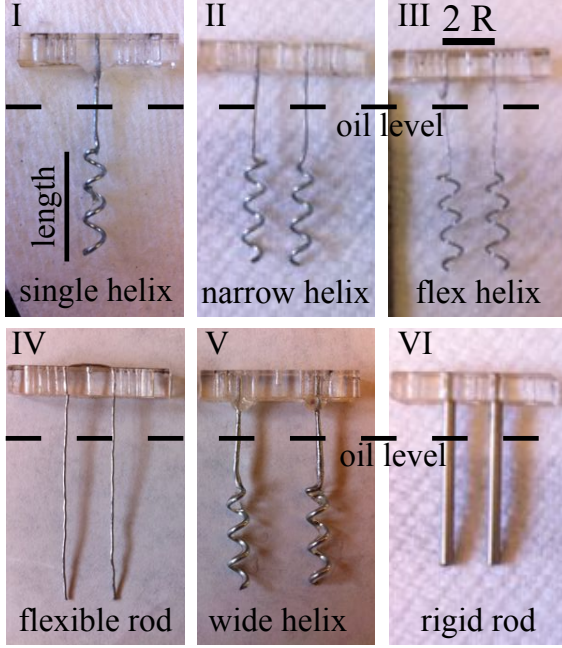| Design	Number	Rigidity	Spacing	Wire diameter
	N	EI (mNm^2)	R (mm)	d (mm)
I	1 helix	1.32	–	0.68
II	2 helices	1.32	3.80	0.68
III	2 helices	0.15	3.80	0.43
IV	2 rods	0.22	3.80	0.43
V	2 helices	1.32	6.35	0.68
VI	2 rods	4.44	3.80	2.00

Fig. 6. The designs used in the experiments. The dotted line shows how far the systems are submerged in silicone oil.

the weight of the cantilever beam and motor. Thus forward motion is prevented to measure the thrust force. For this reason, the rotational, as opposed to translational, Reynolds number is given as

$$Re_{rot} = \frac{\rho f l^2}{\mu} \quad (12)$$

where f is the rotational frequency and ρ is the fluid density. When a single helix is being tested, the amplitude A is used as the characteristic length l. When multiple helices are used, the offset radius R is used as l because it is at this radius that the helices are interacting with the fluid. Bacterial flagella typically operate at $Re_{rot} \approx 10^{-3}$ [10], indicating Stokes flow. Using (12), it is determined, for our geometry, that the offset radius R should be no more than 7.6 mm to simulate a Reynolds number similar to that of the bacteria.

IV. RESULTS

A. Thrust Force

We first test the thrust force of each design when it is rotated at constant frequency. The voltage supply is adjusted to set a rotation speed ω in the range 0.5 to 5.0 Hz. As
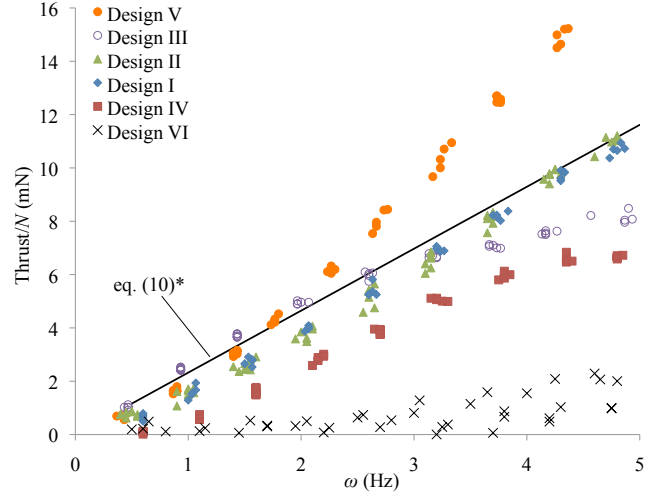

Fig. 7. Experimental results of the thrust force generated at constant frequency by each of the six designs. The thrust is divided by N, the number of helices or rods. The solid black line shows the thrust of a single helix predicted by the model from (10) after being multiplied by the correction factor (11).

shown in Fig. 7, the thrust force generated by the two stiff helices (Design II) is twice that of the single helix (Design I), supporting the hypothesis illustrated in Fig. 3. Both results also agree well with (10), as shown on the plot as a solid black line. Another observation is that the thrust force of the flexible helices (Design III) and flexible rods (Design IV) change non-linearly with frequency. Similar trends have been observed for flexible rods in other works [11].

When testing Design II, no bending is observed and the thrust produced is twice that of a single helix. However, when testing Design V with its larger offset radius, it is observed that the fluidic forces are strong enough to cause significant bending at $\omega \geq 2$ Hz. This deformation leads to a thrust greater than twice that of a single helix for higher frequencies.

The non-linearity of the thrust produced by Design IV results because the thrust force depends on the pitch angle β of the filament [1]. When $\beta = 0°$, thrust equals zero, but thrust reaches a maximum when $35° < \beta < 45°$ [12]. By our definition, the out-of-plane bending angle δ for flexible rods is essentially a pitch angle that varies with ω. Fluidic drag on the filaments causes them to bend out of plane, positively affecting thrust because δ is increased. However, as δ increases the forces acting in plane also increase, thus γ increases. In-plane bending negatively affects thrust because as R decreases, the relative velocity between the filament and fluid decreases ($V(z) = \omega R(z)$). As $V(z)$ decreases, the thrust force also decreases [11]. The bending angles of the flexible rods are measured at four different rotation frequencies and are shown in Table II. It is observed that while γ increases nonlinearly with frequency, δ remains constant above $\omega = 1.70$ Hz. At $\omega = 0.5$ Hz the flexible rods provide negligible thrust because the fluidic forces are not strong enough at that low speed to cause a shape change ($\delta = 0$). At higher speeds it is observed that the rods start to
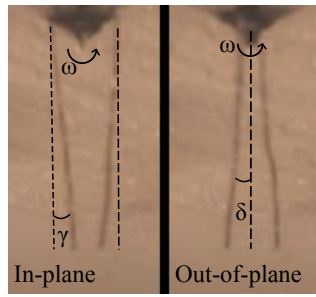
Fig. 8. Photo showing flexible rods (Design IV) bending when rotated at $\omega =4.8$ Hz, as illustrated in Fig. 4. The left shows in-plane bending (γ) and the right shows out-of-plane bending (δ).

TABLE II

MEASURED BENDING ANGLES OF THE FLEXIBLE RODS (DESIGN IV)

DURING ROTATION AT $\omega =4.8$ Hz.

ω (Hz)	0.50	1.70	2.77	3.80	4.80
γ	0°	0°	4°	8°	9°
δ	0°	5°	5°	5°	5°

reach a maximum δ, thus the thrust force does not increase as dramatically from 2 to 4 Hz as it did from 0.5 to 2 Hz.

The non-linearity of the flexible helices in Design III is expected for similar reasons as those given for the flexible rods. However, the flexible helices have the advantage at low speeds because even if they don't bend they still maintain their helical shape. Thus the flexible helices still produce thrust at low speeds while the flexible rods do not. It is observed that the flexible helices approached a maximum bend just like the rods, thus the thrust force tends towards saturation at higher frequencies.

It is expected that Design VI produces negligible thrust because the radius of the rods is large enough that they do not bend under the test conditions. However, the design does produce thrust due to bending at the connection point between the rigid rods and the mount, which is accounted for in the measurement of EI in Table I.

The second series of experiments tests the thrust force of each design as a function of input torque. This is especially relevant for an untethered swimming micro-robot, which is limited by the torque provided by the actuator. The power supply connected to the motor is set to a constant current on the range of 60 to 100 mA with a step of 5 mA. Since the purpose of this experiment is to compare the performance of different designs rather than obtain exact values of the torque required to operate them, the applied torque is simply estimated from the motor's specifications sheet for the appropriate current value. Results from this series of experiments are shown in Fig. 9. It is clear that Design III's flexible helices perform the best out of the five designs for this series of experiments. Design IV's flexible rods and Design II's stiff helices perform no better than the single helix in Design I. The frequencies recorded for these experiments are shown in Fig. 10.

Due to its lower rotational drag, the single helix is able to spin the fastest at lower torques, thus it generates significant
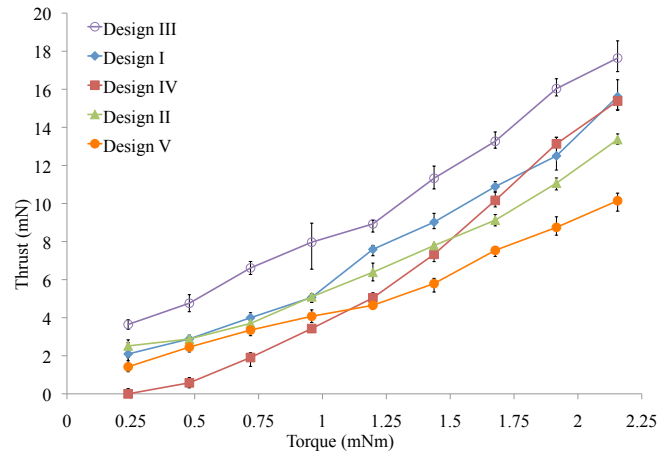

Fig. 9. Experimental results of the thrust forces generated at constant torques by each of the five designs. Error bars are added to show the minimum and maximum measured values, with each point as the mean of five measurements.
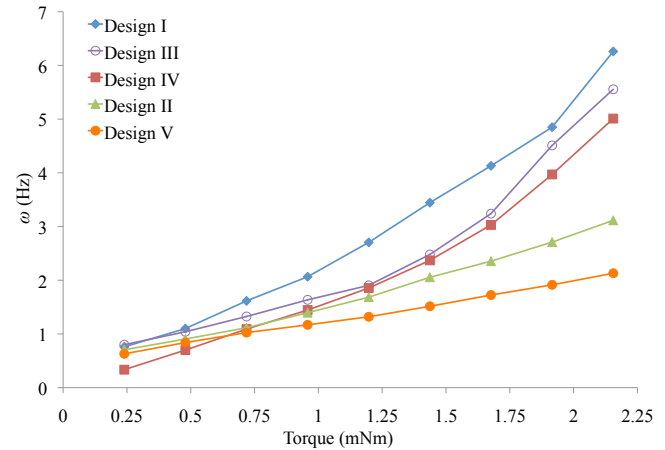

Fig. 10. Experimental results for the average frequencies of rotation at constant torques by each of the five designs. Each point is the mean of five measurements.

thrust. Design II and V require a higher torque to achieve the same rotation frequency as Design I. Thus while the offset helices generate a higher thrust than the single helix when run at the same frequency, the single helix generates more thrust than the offset helices when run at the same torque because the two helices do not rotate as quickly.

Design IV performs the worst because the flexible rods only achieve an adequate shape at higher frequencies. At the lowest applied torque tested, the rods experience no shape change, thus they produce almost no thrust. As torque increases the rods bend more and the propulsive force increases, but the force is still no more than that for the single helix.

The most interesting results are those of Design III. As shown in Fig.10, Design III achieves rotation frequencies similar to those of Design IV, suggesting similar rotational drag. However, the flexible helices produce much higher thrust than all of the other designs. It is speculated that the flexible helices are able to outperform the rods of Design IV due to their geometry, outperform the stiff helices of Designs
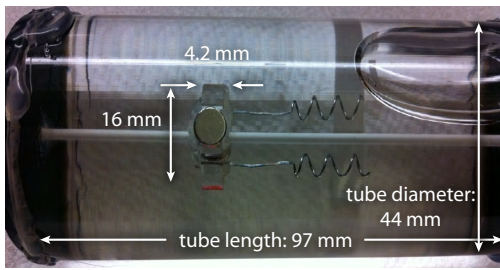
Fig. 11. Photo of the prototype swimming robot inside a tube filled with high viscosity fluid. Video is available in supplementary materials.

II and V due to their flexibility and added benefits from bending effects, and outperform the single helix of Design I simply because there are two of them.

V. MACRO-SCALE PROTOTYPE

A macro-scale prototype is built to test the feasibility of using an external magnetic field to actuate a system that uses flexible offset helices. The miniature robot is untethered and actuated solely by a rotating magnetic field produced by a magnetic coil system. The robot is built from a laser cut acrylic piece, two Neodymium magnets (K&J Magnetics grade N42) with estimated magnetic moment 208 EMU, and the same flexible helices and spacing as Design III.

The robot is submerged in a 44 mm inner diameter, and 96.5 mm length acrylic tube filled with the same 30,000 cSt silicone oil used in the experiments, resulting in a Reynolds number of approximately $Re_{rot} \approx 10^{-3}$. A thin cylindrical rod runs axially through the robot to keep it centered in the tube. A picture of the robot inside the tube is shown in Fig. 11. The tube is placed inside the coil system, which is capable of producing a rotating magnetic field of up to 40 mT in strength. The coil system consists of six independent air-core electromagnetic coils, aligned to the faces of a cube approximately 82 mm on a side. The currents in the electromagnetic coils are controlled using a PC with data acquisition system at a control bandwidth of 10 kHz, using linear electronic amplifiers (SyRen 25, Dimension Engineering Inc.) and Hall-effect current sensors (ACS714, Allegro Microsystems Inc.). The magnitude of the rotating applied field is increased until the robot begins rotating in sync with the field. For a frequency of 3.5 Hz, this requires a field of 35 mT, corresponding to an approximate torque of 15 mNm on the prototype robot.

While the coil system is strong enough to spin the robot at rates up to 3.5 Hz, the magnets are also attracted to the center of the system due to the small size of the coils relative to the prototype. It is observed that this pulling force to the center of the applied magnetic field overpowers the thrust force of the helices. It is likely that the short length of the tube causes forces and fluid flows that affect the robot's progress non-trivially. As the prototype is scaled smaller, we expect the performance to increase because of the reduction in Reynolds number at smaller scales, and the fact that magnetic gradient pulling is less significant.

VI. CONCLUSIONS

While many groups have shown that helical wave propulsion is a suitable technique for micro-scale swimming robots, we have proposed an effective way to increase propulsion using multiple helices without complicating the actuation method. If a micro-robot is actuated by an external field, multiple flexible helices can potentially be used instead of one to generate a higher propulsive force for the same applied magnetic torque. We have shown that doubling the number of helices from one to two effectively doubles the propulsive force while increasing the required applied torque. We have also shown that bending effects can increase propulsion for offset flagella. As future works, fluidic coupling effects among neighboring flagella will be added to the models. We will also compare our multiple helix design to a single large helix with an amplitude equal to the offset radius of the multiple helix design. Our model indicates that amplitude is directly related to thrust, but also related to the number of offset helices. More experiments will be performed to fully understand how the flexibility of helices and their offset distance from the axis of rotation affect propulsion. Moreover, a sub-millimeter scale version of this multi-flagellated swimming robot will be fabricated for potential medical applications in stagnant body fluids.

REFERENCES

[1] B. Behkam and M. Sitti, "Design methodology for biomimetic propulsion of miniature swimming robots," *ASME Journal of Dynamic Systems, Measurement, and Control*, vol. 128, pp. 36–43, 2006.

[2] J. Edd, S. Payen, M. Sitti, M. L. Stoller, and B. Rubinsky, "Biomimetic propulsion mechanism for a swimming surgical micro-robot," in *Proc. IEEE. Int. Conf. on Int. Rob. and Sys.*, Las Vegas, USA, 2003, pp. 2583–88.

[3] B. Nelson, I. Kaliakatsos, and J. Abbott, "Microrobots for minimally invasive medicine." *Ann. Rev. of Biom. Eng.*, vol. 12, pp. 55–85, 2010.

[4] J. Lighthill, "Flagellar hydrodynamics," *SIAM Review*, vol. 18, pp. 161–230, 1976.

[5] L. Zhang, J. Abbott, L. Dong, K. Peyer, B. Kratochvil, H. Zhang, C. Bergeles, and B. Nelson, "Characterizing the swimming properties of artificial bacterial flagella," *Nano Lett.*, vol. 9, pp. 3663–3667, 2009.

[6] J. Gibbs and Y. Zhao, "Catalytic nanomotors: fabrication, mechanism, and applications," *Front. of Mat. Sc.*, vol. 5, pp. 25–39, 2011.

[7] J. Abbott, K. Peyer, M. Lagomarsino, L. Zhang, L. Dong, I. Kaliaktsos, and B. Nelson, "How should microrobots swim?" *The Int. J. of Rob. Res.*, vol. 28, pp. 1434–47, 2009.

[8] A. Ghosh and P. Fischer, "Controlled propulsion of artificial magnetic nanostructured propellers," *Nano Lett.*, vol. 9, pp. 2243–2245, 2009.

[9] V. Arabagi, B. Behkam, E. Cheung, and M. Sitti, "Modeling of stochastic motion of bacteria propelled spherical microbeads," *J. of App. Phys.*, vol. 109, p. 114702, 2011.

[10] C. Brennen and H. Winet, "Fluid mechanics of propulsion by cilia and flagella," *Ann. Rev. Fluid Mech.*, vol. 9, pp. 339–398, 1977.

[11] B. Qian, T. R. Powers, and K. S. Breuer, "Shape transition and propulsive force of an elastic rod rotating in a viscous fluid," *Phys. Rev. Lett.*, vol. 100, pp. 078 101–4, 2008.

[12] B. Behkam and M. Sitti, "E. coli inspired propulsion for swimming microrobots," in *ASME Int. Mech. Eng. Cong. and Expo.*, Anaheim, USA, 2004, p. 59621.